photonics

MDPI

Article

Intensity-Difference Squeezing in a Fiber Nonlinear Interferometer: Theoretical Optimization and Experimental Realization

Nan Huo , Xinyue Lv, Jinze Wu and Jing Wang *

Shanxi Center of Technology Innovation for Light Manipulations and Applications, School of Applied Science, Taiyuan University of Science and Technology, Taiyuan 030024, China; huonan@tyust.edu.cn (N.H.)
* Correspondence: wangjingty@tyust.edu.cn

Abstract

Nonlinear interferometers offer a robust platform for quantum sensing beyond the standard quantum limit. Specifically, the generation of high-quality intensity-difference-squeezed (IDS) states provides a distinct advantage by circumventing the need for complex phase-coherent local oscillators. However, practical imperfections such as asymmetric inter-stage transmission and unbalanced detection losses severely degrade the generation of these states. In this work, we analyze IDS state generation within fiber nonlinear interferometers utilizing cascaded parametric amplifiers. Using a single-mode theoretical framework and experimental demonstration, we derive an optimal electronic gain ratio for differential detection to compensate for asymmetric detection-induced noise mismatches, extending achievable squeezing into the high-gain regime. We further analyze system tolerance to inter-stage losses and path delays. Experiments demonstrate that while higher initial parametric gain improves quantum correlations, it amplifies intensity noise and accelerates gain saturation, resulting in optimal squeezing at balanced low-gain configurations. These findings establish a robust framework for the design and optimization of all-fiber quantum sensors.

Keywords: fiber nonlinear interferometer; intensity-difference squeezed states; asymmetric inter-stage transmission; detection losses; quantum sensors

1. Introduction

With the rapid advancement of quantum information science, quantum precision measurement has emerged as a prominent frontier in both physics and engineering [1]. By exploiting the non-classical properties of optical fields, such as entanglement and squeezing, researchers can achieve measurement sensitivities beyond the standard quantum limit (SQL). This capability holds immense potential for applications including weak force detection, gravitational wave observation, biological imaging, and sub-shot-noise phase measurement [2,3]. Among various continuous-variable quantum states, the intensity-difference-squeezed (IDS) state, commonly referred to as twin beams, has attracted significant interest due to its strong non-classical intensity correlations [4]. In practice, IDS significantly advances high-sensitivity measurements. For example, it has enabled high-precision raster-scanning microscopy, sub-shot-noise quantum imaging, and stimulated Brillouin scattering spectroscopy with sensitivities well below the SQL [5–8]. Compared with quadrature-squeezed states, IDS detection circumvents the need for a complex phase-coherent local oscillator. Substantial suppression of quantum noise can be achieved simply via direct detection of the intensity difference between the signal and idler beams, signif-

Check for updates

Received: 27 June 2026
Revised: 23 July 2026
Accepted: 24 July 2026
Published: 30 July 2026

Copyright: © 2026 by the authors. Licensee MDPI, Basel, Switzerland. This article is an open access article distributed under the terms and conditions of the Creative Commons Attribution (CC BY) license.

icantly simplifying the configuration and reducing the implementation cost of practical quantum sensing systems [9,10].

Traditionally, IDS states are generated using a single-stage optical parametric amplifier (OPA) via spontaneous parametric down-conversion or four-wave mixing (FWM) [11]. Although demonstrated in atomic vapors and all-fiber platforms operating within telecommunication bands, single-stage architectures are fundamentally constrained by their extreme susceptibility to external losses [12–15]. Even marginal dissipation couples vacuum fluctuations into the system, severely degrading the squeezing. Furthermore, the intrinsic lack of phase-sensitive coherent pre-amplification in single-stage architectures leaves the signal readout highly vulnerable to classical detection noise in practical metrology. To circumvent these bottlenecks, nonlinear interferometers (NLIs) formed by coherently cascading two OPAs have emerged as a robust alternative [16,17]. NLIs harness precise quantum interference for coherent noise cancelation at specific operating phases [18]. This phase-sensitive amplification concurrently enhances quantum correlations, phase sensitivity, and resilience against detection losses in ideal configurations [19–22]. However, maintaining such robustness under realistic asymmetric loss conditions requires novel compensation strategies.

Integrating non-classically correlated states into practical measurement schemes holds significant promise for precision metrology. Beyond circumventing the limitations of infrared detectors, NLIs are highly attractive for their theoretical robustness against environmental and detection losses [23–26]. For broader applications in photonic information and advanced sensing, it is important to distinguish this NLI-based quantum approach from emerging classical technologies such as optical microcombs. Microcombs provide compact frequency rulers, wavelength-parallel channels, and time-frequency resources, and their state-of-the-art sensing mechanisms primarily rely on multi-wavelength readouts and frequency-to-sensing mapping [27,28]. In contrast, NLIs address distinct system-level needs by targeting sub-shot-noise measurements. Specifically, the present IDS-based NLI configuration achieves sensitivity enhancements fundamentally through the direct suppression of correlated intensity noise. However, while the existing literature predominantly focuses on optimizing NLI phase sensitivity, a systematic analysis of how internal system parameters govern the achievable IDS remains largely unexplored. Specifically, pulse-pumped fiber OPAs possess inherent multimode complexity due to their broadband interacting fields [29]. In practical all-fiber cascaded configurations, this complexity is compounded by systematic imperfections such as inter-stage path differences, asymmetric transmission losses, and unbalanced photodetector efficiencies, all of which inevitably induce a severe quantum noise unbalance between output ports [30]. In the high-gain regime, this mismatch couples excess noise and anti-squeezing into the detection channels, fundamentally constraining measurable squeezing levels and hindering the transition of NLIs from proof-of-principle demonstrations to engineered quantum sensors.

To address these challenges, this paper presents a systematic theoretical simulation and experimental demonstration of IDS state generation based on a pulsed-pumped all-fiber NLI. By constructing a high-performance cascaded OPA system, we explore the joint effects of critical parameters on IDS quality, aiming to provide a highly stable, integrated, and deeply squeezed quantum light source for precision metrology. First, we analyze the joint impact of the OPA amplitude gain factors (g_1, g_2). By comparing squeezing distributions under standard ($r = 1$) and optimized (r_{opt}) electronic gain ratios, we demonstrate how optimized photoelectric detection fundamentally mitigates noise mismatch induced by system asymmetries. Second, we investigate the sensitivity of IDS to inter-stage transmission efficiencies, evaluating squeezing degradation under localized losses in the idler arm versus simultaneous losses in both arms. Furthermore, we explore the temporal dynamics

of the system by analyzing the impact of a physical inter-stage path delay. Experimentally, we validate these theoretical models by investigating the dependence of IDS evolution on OPA2 pump power across various OPA1 idler intensity gains under the optimized condition ($r = r_{\mathrm{opt}}$). Finally, we quantify the system's resilience to practical imperfections by evaluating squeezing under extreme conditions: complete blockage of the inter-stage idler beam and the introduction of a discrete path delay corresponding to the adjacent-pulse interval. Collectively, this work bridges the gap between ideal cascaded models and systematic imperfections, offering a framework for designing robust and practical quantum sensing systems.

2. Theoretical Methods

The schematic diagram is shown in Figure 1, where the NLI consists of OPA1 and OPA2. The signal $\hat{a}_s$ and idler $\hat{a}_i$, with corresponding amplitudes $|\alpha\rangle$ and $|\beta\rangle$, are injected into the OPA1; the input–output relationship of the parametric process can be expressed as [16,17] ,

$$a_{s1} = G_1\hat{a}_s + e^{i\varphi_1}g_1\hat{a}_i^{\dagger}, \tag{1}$$

$$a_{i1} = G_1\hat{a}_i + e^{i\varphi_1}g_1\hat{a}_s^{\dagger}, \tag{2}$$

where G_1 and g_1 with $G_1^2 - g_1^2 = 1$ are the amplitude gains of OPA1, the signal input is in a coherent state, and the idler input can be either in a coherent or vacuum state. φ_1 is the relative phase of the input field of OPA1.

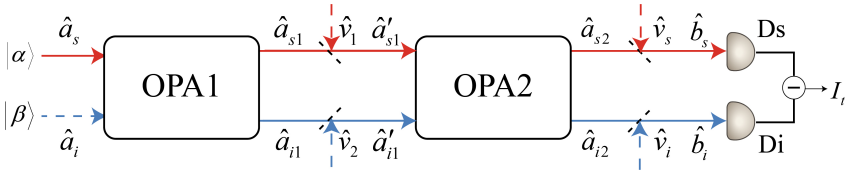


Figure 1. Schematic diagram of NLI based on two OPAs. OPA1-2, optical parametric amplifier; $\mathrm{D}_{s(i)}$, detector. The signal field $\hat{a}_s$ and idler field $\hat{a}_i$ are injected into OPA1 with a coherent state $|\alpha| > 0$ and vacuum state $|\beta| = 0$, respectively. The beam splitters at the dashed lines are used to model the photon losses in the system, thereby introducing the corresponding vacuum noise ($\hat{v}_1$, $\hat{v}_2$, $\hat{v}_s$, $\hat{v}_i$). After OPA2, the final intensity difference signal I_t is output via differential detection.

In practice, internal losses between the cascaded parametric amplifiers inevitably degrade the quantum correlation. By incorporating the standard beam splitter (BS) model with transmission efficiencies η_1 and η_2, the intermediate field operators propagating into OPA2, denoted by $\hat{a}'_{s1}$ and $\hat{a}'_{i1}$, are linearly coupled with vacuum noise. Consequently, the input–output relationships of OPA2 (with a phase shift φ_2) can be directly expressed as:

$$\begin{aligned}\hat{a}_{s2} &= G_2\hat{a}'_{s1} + e^{i\varphi_2}g_2\hat{a}'^{\dagger}_{i1} \\ &= G_s\hat{a}_s + g_s\hat{a}_i^{\dagger} + \sqrt{1-\eta_1}G_2\hat{v}_1 + \sqrt{1-\eta_2}e^{i\varphi_2}g_2\hat{v}_2^{\dagger},\end{aligned} \tag{3}$$

$$\begin{aligned}\hat{a}_{i2} &= G_2\hat{a}'_{i1} + e^{i\varphi_2}g_2\hat{a}'^{\dagger}_{s1} \\ &= G_i\hat{a}_i + g_i\hat{a}_s^{\dagger} + \sqrt{1-\eta_2}G_2\hat{v}_2 + \sqrt{1-\eta_1}e^{i\varphi_2}g_2\hat{v}_1^{\dagger},\end{aligned} \tag{4}$$

where G_2 and g_2 with $G_2^2 - g_2^2 = 1$ are the amplitude gains of OPA2, $\hat{v}_1$ and $\hat{v}_2$ denote the vacuum fields coupled via the unused BS ports. The effective amplitude gains of the cascaded system are given by

$$G_s = \sqrt{\eta_1}G_2G_1 + \sqrt{\eta_2}e^{i(\varphi_2-\varphi_1)}g_2g_1^*, \quad g_s = \sqrt{\eta_1}e^{i\varphi_1}G_2g_1 + \sqrt{\eta_2}e^{i\varphi_2}g_2G_1^*, \tag{5}$$

$$G_i = \sqrt{\eta_2}G_2G_1 + \sqrt{\eta_1}e^{i(\varphi_2-\varphi_1)}g_2g_1^*, \quad g_i = \sqrt{\eta_2}e^{i\varphi_1}G_2g_1 + \sqrt{\eta_1}e^{i\varphi_2}g_2G_1^*. \tag{6}$$

The generated signal and idler fields were measured using detectors D_s and D_i. The average photon number $I_{s(i)}$ and the photon-number fluctuation $\Delta I^2_{s(i)}$ of the signal (idler) fields are converted to the direct current (DC) and alternating current (AC) of D_s and D_i, respectively. When the transmission and detection efficiencies of the detectors are ideal, the average photon numbers of the signal and idler fields can be written as

$$I_s = \langle \hat{a}^\dagger_{s2}\hat{a}_{s2}\rangle, \quad \Delta I_s^2 = \langle (\hat{a}^\dagger_{s2}\hat{a}_{s2})^2\rangle - \langle \hat{a}^\dagger_{s2}\hat{a}_{s2}\rangle^2, \tag{7}$$

$$I_i = \langle \hat{a}^\dagger_{i2}\hat{a}_{i2}\rangle, \quad \Delta I_i^2 = \langle (\hat{a}^\dagger_{i2}\hat{a}_{i2})^2\rangle - \langle \hat{a}^\dagger_{i2}\hat{a}_{i2}\rangle^2 \tag{8}$$

In practical experimental scenarios, the output fields from the NLI experience additional propagation losses and non-ideal quantum efficiencies, collectively characterized as detection efficiencies η_s and η_i. Modeling these imperfections via standard BS transformations, the field operators arriving at the detectors, denoted by $\hat{b}_s$ and $\hat{b}_i$, are coupled with vacuum noise operators $\hat{v}_s$ and $\hat{v}_i$. The measured average photon numbers are thus given by

$$I_s^{'} = \langle \hat{b}^\dagger_s \hat{b}_s\rangle = \eta_s I_s = \eta_s(|G_s|^2|\alpha|^2 + G_s^* g_s \alpha^* \beta^* + g_s^* G_s \alpha\beta + |g_s|^2(|\beta|^2+1) + |g_2|^2(1-\eta_2)), \tag{9}$$

$$I_i^{'} = \langle \hat{b}^\dagger_i \hat{b}_i\rangle = \eta_i I_i = \eta_i(|G_i|^2|\beta|^2 + G_i^* g_i \beta^* \alpha^* + G_i g_i^* \alpha\beta + |g_i|^2(|\alpha|^2+1) + |g_2|^2(1-\eta_1)), \tag{10}$$

and the intensity noise of the individual signal and idler fields are written as

$$\Delta(I_s')^2 = \langle (\hat{b}^\dagger_s \hat{b}_s)^2\rangle - \langle \hat{b}^\dagger_s \hat{b}_s\rangle^2 = \eta_s^2 \Delta I_s^2 + \eta_s I_s - \eta_s^2 I_s, \tag{11}$$

$$\Delta(I_i')^2 = \langle (\hat{b}^\dagger_i \hat{b}_i)^2\rangle - \langle \hat{b}^\dagger_i \hat{b}_i\rangle^2 = \eta_i^2 \Delta I_i^2 + \eta_i I_i - \eta_i^2 I_i, \tag{12}$$

When measuring the IDS generated by the NLI, the practical response functions of the detection system must be carefully considered. We characterized the overall response functions of the two detectors as $Q_s(\Omega)$ and $Q_i(\Omega)$, where Ω represents the radio frequency. The DC response of the detectors, $Q_{s(i)}(0)$, is fundamentally determined by their quantum efficiencies through the relation $Q_{s(i)}(0) = \frac{e\eta_{s(i)}}{\hbar\omega}$, where e is the elementary charge, $\eta_{s(i)}$ is the detection efficiency of $D_{s(i)}$ (if the transmission efficiency is ideal, $\eta_{s(i)}$ is the quantum efficiency of the detector), and $\hbar\omega$ is the photon energy. Conversely, the AC response $Q_{s(i)}(\Omega)$ in the high-frequency regime ($\Omega \neq 0$) is governed not only by the intrinsic high-frequency response of the respective photodiodes $D_{s(i)}(\Omega)$ but also by the electronic gain of the subsequent radio-frequency amplifiers $A_{s(i)}(\Omega)$. To accurately evaluate the degree of IDS, characterizing the asymmetry between the two detection channels is crucial. For convenience, the AC response ratio r between D_s and D_i is defined as

$$r(\Omega) = \frac{\eta_s A_s(\Omega) D_s(\Omega)}{\eta_i A_i(\Omega) D_i(\Omega)} \quad (\Omega \neq 0) \tag{13}$$

Experimentally, r can be optimized by adjusting A_s or A_i. The measured intensity difference operator for the twin beams is then formulated as $\hat{I}_t = \hat{b}^\dagger_s \hat{b}_s - r\hat{b}^\dagger_i \hat{b}_i$. Consequently, the intensity difference noise variance is evaluated as

$$\Delta I_t^2 = \langle (\hat{b}^\dagger_s \hat{b}_s - r\hat{b}^\dagger_i \hat{b}_i)^2\rangle - \langle \hat{b}^\dagger_s \hat{b}_s - r\hat{b}^\dagger_i \hat{b}_i\rangle^2 = \Delta(I_s')^2 + r^2\Delta(I_i')^2 - rH_{si} - rH_{is}, \tag{14}$$

where H_{si} and H_{is} denote the quantum correlation terms. Normalizing this variance against the shot noise limit (SNL) yields [13]

$$R_t = \frac{\Delta I_t^2}{\Delta(I_{cs}')^2 + r^2\Delta(I_{ci}')^2} = \frac{\Delta(I_s')^2 + r^2\Delta(I_i')^2 - rH_{si} - rH_{is}}{I_s' + r^2 I_i'}, \tag{15}$$

where $\Delta(I'_{cs,ci})^2 = I'_{s,i}$ represents the corresponding SNL of the detected signal and idler fields.

The analysis in this paper is conducted under the single-mode theory, although pulse-pumped fiber parametric processes are fundamentally multimode in nature, characterized by intricate joint spectral functions and multi-frequency coupling. A single-mode theoretical framework is implemented here as a primary formulation to transparently distill the foundational physics of cascaded quantum interference and loss compensation [29]. To study the factors affecting the intensity noise R_t, we first consider that OPA1 is phase non-sensitive, that is, $|\alpha| \gg 0$, $|\beta| = 0$. At this point, the output intensity of the NLI varies with the relative phase φ_2 between OPA1 and OPA2. To obtain the IDS, the phase should be locked to the position of the bright beam, that is, $\varphi_2 = 0$. Assuming that the inter-stage transmission efficiencies η_1 and η_2 are ideal, the ratio r is equal to 1, and by varying the detection efficiencies η_s and η_i, the variation of R_t with g_1 and g_2 is shown in the contour maps in Figure 2. The efficiencies of D_s and D_i can each independently be 85% or 80%, and the contour lines reflect the partial IDS values. As shown in Figure 2a, when the efficiencies of D_s and D_i are both fixed at 85%, the values of IDS can reach a relatively large value within the range where g_1 and g_2 are both greater than 1. As the amplitude gains increase, the increase in the IDS values gradually slows down. However, in Figure 2b,c, the unbalance in the detection efficiency causes the IDS value to take a larger value within a certain gain range. Comparing Figure 2b,c, it can be seen that when the detection efficiency of the signal beam is lower than that of the idler beam, it is easier to obtain a larger IDS value. This is because we assume that the injected signal field has $|\alpha\rangle > 0$, and the parametric amplification process in the NLI adds excess noise to the signal beam.

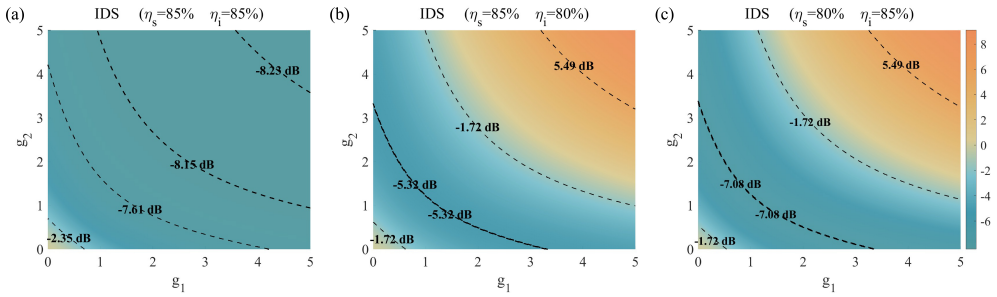


Figure 2. Numerical simulation of the IDS as a function of the amplitude gain factors g_1 and g_2 for $r = 1$ under different detection efficiencies (**a**) $\eta_s = \eta_i = 85\%$, (**b**) $\eta_s = 85\%$ and $\eta_i = 80\%$, (**c**) $\eta_s = 80\%$ and $\eta_i = 85\%$. The dashed lines represent the specific contour levels of squeezing in the logarithmic scale.

From Equation (15), we can infer that R_t is related to the given values of η_1, η_2, η_s, η_i, g_1 and g_2. R_t can take the extreme value when the ratio r takes the optimized value:

$$r_{\text{opt}} = \frac{(I'_i\Delta I'^2_s - \Delta I'^2_i I'_s) \pm \sqrt{(I'_i\Delta I'^2_s - \Delta I'^2_i I'_s)^2 + I'_i I'_s (H_{si} + H_{is})^2}}{I'_i(H_{si} + H_{is})} \tag{16}$$

According to the above expression, we plotted R_t as a function of g_1 and g_2 by maintaining the same detection efficiency combinations as in Figure 2. Figure 3 illustrates the simulated IDS contour maps for $r = r_{\text{opt}}$. As illustrated in Figure 3a, with the efficiencies of D_s and D_i symmetrically fixed at 85%, the IDS level is monotonically enhanced with the increase of g_1 and g_2. Although the overall evolution profile is consistent with that in the $r = 1$ case, using the optimized gain ratio enables the system to achieve equivalent squeezing levels at lower parametric amplitude gains. The introduction of unbalanced detection efficiencies yields the distinct profiles shown in Figure 3b,c. In contrast to the unoptimized condition, the IDS level continuously improves as both amplitude gains scale

up. Furthermore, the exact equivalence of the squeezing contours in Figure 3b,c verifies that applying the optimal gain ratio $r = r_{\text{opt}}$ makes the intensity noise R_t independent of the specific assignment of channel efficiencies. Consequently, this inherent symmetry provides the system with enhanced robustness against asymmetric channel losses.

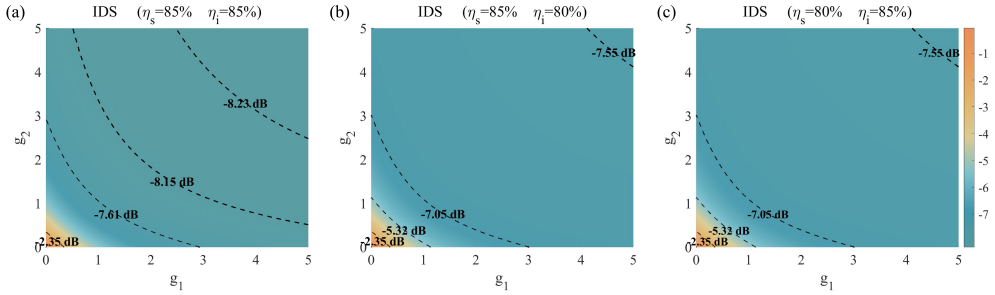


Figure 3. Numerical simulation of the IDS as a function of the amplitude gain factors g_1 and g_2 for $r = r_{\text{opt}}$ under different detection efficiencies (**a**) $\eta_s = \eta_i = 85\%$, (**b**) $\eta_s = 85\%$ and $\eta_i = 80\%$, (**c**) $\eta_s = 80\%$ and $\eta_i = 85\%$. The dashed lines represent the specific contour levels of squeezing in the logarithmic scale.

A comparison between Figure 2 ($r = 1$) and Figure 3 ($r = r_{\text{opt}}$) elucidates the physical mechanism by which the optimized ratio preserves the squeezing performance under unbalanced conditions. For balanced detection efficiencies [Figures 2a and 3a], the contour maps are qualitatively similar, as the symmetric channel configuration yields an optimal ratio approaching unity ($r_{\text{opt}} \approx 1$). However, in the presence of asymmetric detection losses, the squeezing characteristics exhibit a significant departure, most notably in the high-gain regime. When fixing $r = 1$ under these conditions [Figure 2b,c], the excess noise from the parametric amplification process introduces a substantial unbalance between the twin beams. As g_1 and g_2 scale up, this noise asymmetry accelerates the deterioration of quantum correlations, confining high IDS levels to a narrow, low-gain region. Conversely, by adopting $r = r_{\text{opt}}$ [Figure 3b,c], the differential photon losses are effectively compensated in the electronic domain. Consequently, the degradation in the high-gain regime is substantially suppressed, enabling the system to sustain strong quantum correlations and achieve improved IDS performance across a broader parameter space.

In fact, in NLI-based applications for quantum precision measurement and quantum sensing, the optical loss inevitably introduced by inserting the probe sample between two amplifiers has a critical impact on the overall performance. Such samples are placed between the two OPAs and can introduce either symmetric or asymmetric inter-stage losses. In extreme cases, one of the arms may become completely opaque. Figure 4 illustrates the dependence of IDS on the amplitude gains g_1 and g_2 under three distinct inter-stage efficiency configurations, assuming detection efficiencies of 85% for both channels, and the ratio r is optimal ($r = r_{\text{opt}}$). Figure 4a depicts an asymmetric loss scenario ($\eta_1 = 100\%$, $\eta_2 = 50\%$) where the sample attenuates only the idler arm. Although the quantum correlation of the output field from OPA1 is partially attenuated, a high degree of IDS (e.g., exceeding -7.95 dB under current conditions) is still preserved in the high-gain regime, demonstrating the robustness of the NLI when coupled with optimal gain tuning. The results of the extreme sensing case, where the sample is completely opaque ($\eta_1 = 100\%$, $\eta_2 = 0\%$), are shown in Figure 4b. Physically, the complete absorption in the idler arm entirely severs the quantum correlation established by the OPA1. Consequently, OPA2 is seeded by the amplified signal field from OPA1 but is driven by a vacuum state in the idler port. This phase-insensitive amplification of uncorrelated noise degrades the squeezing, confining the optimal IDS to a reduced parameter space and requiring a gain unbalance to achieve quantum advantage. Finally, Figure 4c shows the symmetric loss ($\eta_1 = 50\%$,

$\eta_2 = 50\%$), similar to a balanced sensing configuration where the sample imparts equal attenuation to both arms. A comparison between Figure 4a,c reveals that while symmetric attenuation introduces a higher internal loss, the trend of the IDS contours remains similar. Ultimately, these results indicate that while inter-stage attenuation inevitably constrains the maximum achievable IDS values, we can strategically extract the optimal quantum-enhanced measurement sensitivity by carefully tailoring the parametric gain regime.

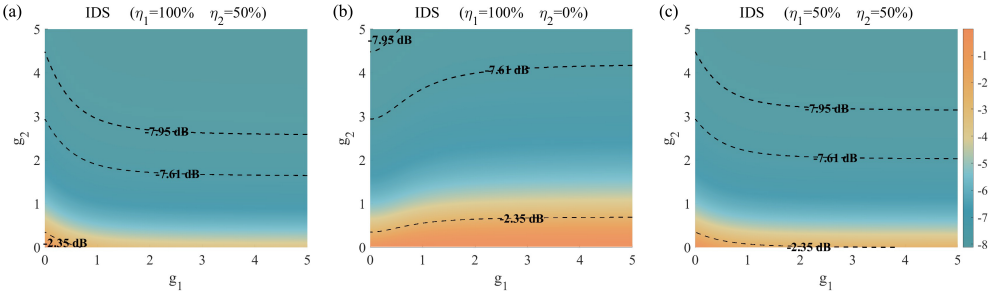


Figure 4. Numerical simulation of the IDS as a function of the amplitude gain factors g_1 and g_2 for $r = r_{\text{opt}}$ and detector efficiencies of $\eta_s = 85\%$ and $\eta_i = 85\%$. (**a**) Asymmetric inter-stage transmission efficiency with $\eta_1 = 100\%$ and $\eta_2 = 50\%$. (**b**) Asymmetric inter-stage transmission efficiency with $\eta_1 = 100\%$ and $\eta_2 = 0\%$. (**c**) Symmetric inter-stage transmission efficiency with $\eta_1 = 50\%$ and $\eta_2 = 50\%$. The dashed lines represent specific contour levels of squeezing in the logarithmic scale.

To evaluate the practical application of the NLI, it is essential to account for the inevitable optical path delay introduced by placing a physical sample between two OPAs. During the inter-stage propagation, these fields experience asymmetric transmission efficiencies η_1 and η_2, evolving into the intermediate fields $\hat{a}_{s1}^{\prime(j)}$ and $\hat{a}_{i1}^{\prime(j)}$ (which implicitly incorporate the corresponding vacuum noise contributions). Furthermore, introducing an interval ΔT between two adjacent pulses in the idler arm corresponds to a phase shift e^{ikL} and causes the j-th pulse of the signal to couple with the $(j-1)$-th pulse of the idler at OPA2. Equations (1)–(4) can be replaced with

$$\hat{a}_{s1}^{(j)} = G_1 \hat{a}_s^{(j)} + e^{i\varphi_1} g_1 \hat{a}_i^{(j)\dagger}, \qquad \hat{a}_{i1}^{(j)} = G_1 \hat{a}_i^{(j)} + e^{i\varphi_1} g_1 \hat{a}_s^{(j)\dagger}, \tag{17}$$

$$\hat{a}_{s2}^{(j)} = G_2 \hat{a}_{s1}^{\prime(j)} + e^{i\varphi_2} e^{ikL} g_2 \hat{a}_{i1}^{\prime(j-1)\dagger}, \qquad \hat{a}_{i2}^{(j-1)} = e^{-ikL} G_2 \hat{a}_{i1}^{\prime(j-1)} + e^{i\varphi_2} g_2 \hat{a}_{s1}^{\prime(j)\dagger}. \tag{18}$$

The superscript (j) denotes the pulse index. After calculation, Equations (5) and (6) can be expressed as

$$G_s = \sqrt{\eta_1}\, G_2 G_1 + \sqrt{\eta_2}\, e^{i(\varphi_2 - \varphi_1)} e^{ikL} g_2 g_1^*, \quad g_s = \sqrt{\eta_1}\, e^{i\varphi_1} G_2 g_1 + \sqrt{\eta_2}\, e^{i\varphi_2} e^{ikL} g_2 G_1^*, \tag{19}$$

$$G_i = \sqrt{\eta_2}\, e^{-ikL} G_2 G_1 + \sqrt{\eta_1}\, e^{i(\varphi_2 - \varphi_1)} g_2 g_1^*, \quad g_i = \sqrt{\eta_2}\, e^{i\varphi_1} e^{-ikL} G_2 g_1 + \sqrt{\eta_1}\, e^{i\varphi_2} g_2 G_1^*. \tag{20}$$

It can be seen that, within the framework of single-mode theory, the optical path delay effectively introduces an additional phase shift e^{ikL} to the NLI amplitude gain factors. The subsequent calculations of the output port intensity and noise are similar to those without delay; they only require an analysis of the impact of the theoretically introduced phase shift on IDS.

To isolate the effect of this inter-stage delay on the IDS and exclude the influence of system losses, we assumed an ideal inter-stage transmission efficiency and fixed the detection efficiencies of 85% for both the signal and idler. Without loss of generality, Figure 5a,b illustrate the dependence of the IDS on g_2 for different delay lengths L introduced in the idler arm. The selected lengths corresponded to the absence of a sample ($L = 0$ m), a short sample length ($L = 0.1$ m), and a distance approximating the separation between adjacent mode-locked pulses in the fiber ($L = 4.08$ m), respectively. Here, g_1 is fixed at a relatively

high value of 5, to ensure strong quantum correlations in the output fields of OPA1. While Figure 5a depicts a symmetric gain ratio configuration ($r = 1$), Figure 5b shows the optimal case ($r = r_{opt}$). A comparison revealed that the difference in the IDS values was noticeable only in the low-gain regime, and the curves converged and became almost indistinguishable at higher gains. Notably, the ideal zero-delay case ($L = 0$ m) maintains maximum squeezing. A short delay ($L = 0.1$ m) destroys the temporal overlap of the interacting pulses in OPA2, severely degrading the IDS. However, setting $L = 4.08$ m effectively recovers the squeezing by synchronizing the delayed idler with the subsequent pump and signal pulses. The slight deviation between the $L = 4.08$ m and $L = 0$ m curves arises because 4.08 m is an approximated separation, which introduces a minor temporal mismatch, leading to incomplete mode overlap and a slight reduction in interference efficiency. Figure 5c,d present an alternative strategy for scenarios in which precisely tuning r to r_{opt} is experimentally challenging. By adopting a symmetric coherent state injection ($|\alpha| = |\beta| > 0$), OPA 1 operated effectively in a phase-sensitive regime. Under this condition, the simplified symmetric configuration ($r = 1$) [Figure 5c] achieves a performance identical to that of the optimally tuned configuration ($r = r_{opt}$) [Figure 5d]. In essence, rather than optimizing the ratio r, this approach relies on modifying the input light to make the OPA1 phase-sensitive, which consequently shifts the experimental requirement to rigorous phase stabilization. Through calculations based on our theoretical models, we established that the relative phases of the input fields for both OPA1 and OPA2 must be precisely locked to 0, which corresponds to the bright fringe condition. Despite the increased complexity of phase management, attaining an optimal IDS remains experimentally feasible, provided that the phase-locking system is sufficiently stable.

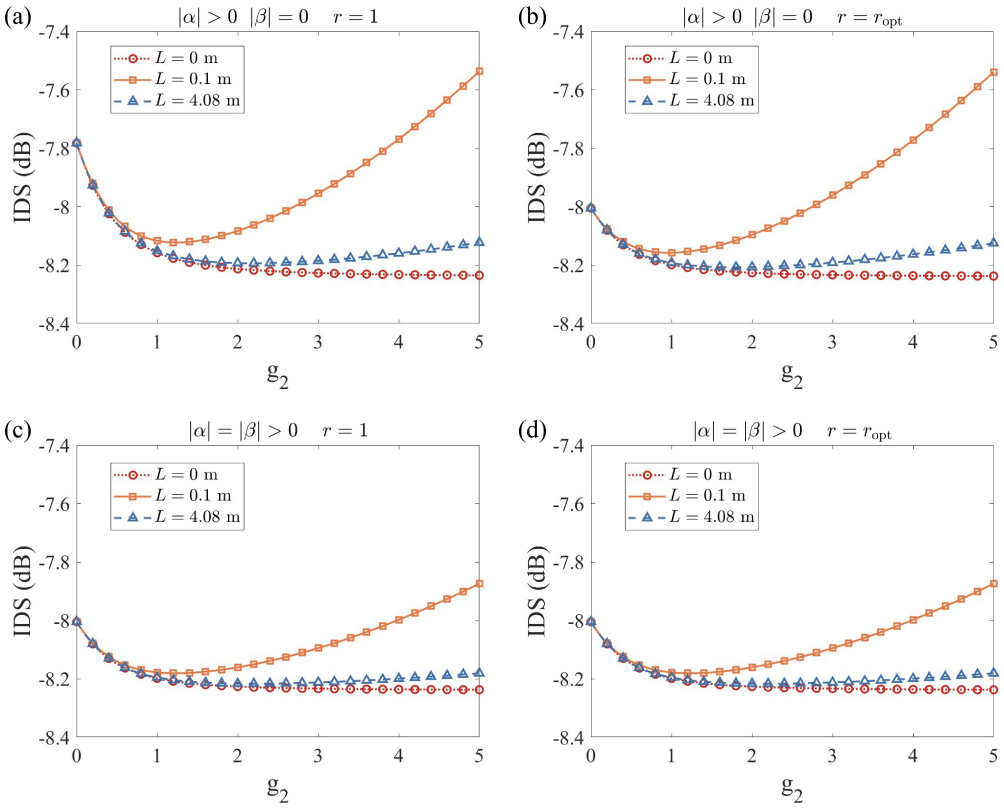


Figure 5. Numerical simulation of the IDS as a function of g_2 for different delay lengths L introduced on the idler arm between OPA 1 and OPA 2. The selected lengths correspond to the absence of a sample ($L = 0$ m), the introduction of a short sample ($L = 0.1$ m), and a distance approximating the

separation between adjacent mode-locked pulses in the fiber ($L = 4.08$ m). (**a**,**b**) Single-mode coherent input ($|\alpha| > 0, |\beta| = 0$), corresponding to a phase-insensitive OPA1, under $r = 1$ and $r = r_{\text{opt}}$, respectively. (**c**,**d**) Symmetric two-mode coherent input ($|\alpha| = |\beta| > 0$), corresponding to a phase-sensitive OPA1, under $r = 1$ and $r = r_{\text{opt}}$, respectively.

3. Experimental Demonstration

The experimental setup for generating the IDS state based on the NLI is illustrated in Figure 6. The pulse train generated by a mode-locked laser (repetition rate 50 MHz, central wavelength 1560 nm) was filtered and divided into a pump field, an injected signal, and an idler field. The pump field was further split to drive OPA1 and OPA2. Both OPAs consisted of 150 m of dispersion-shifted fiber (DSF1 and DSF2) and coarse-wavelength division multiplexers (CWDMs). To suppress spontaneous Raman scattering, the DSFs were immersed in liquid nitrogen at 77 K. The pump pulses for both OPAs (Pump 1 and Pump 2) shared a central wavelength of 1549.32 nm and a 3 dB bandwidth of 0.5 nm, and were amplified by using erbium-doped fiber amplifier (EDFA). For OPA1, the injected signal (1532.5 nm) and idler (1566.5 nm) fields, each with a bandwidth of 1.2 nm, were multiplexed with Pump 1 via CWDM1 and launched into DSF1. OPA1 can operate as either a phase-insensitive or phase-sensitive amplifier (PIA/PSA) by selectively injecting the idler field via a flip mirror (F). After separation from Pump 1 via CWDM2, the correlated signal and idler fields generated by OPA1 were directly injected into OPA2 to drive it as a PSA. Prior to entering OPA2, Pump 2 was phase-modulated by a piezoelectric transducer (PZT), recombined with the OPA1 output via CWDM3, and co-propagated through DSF2. Finally, the output fields from the NLI were separated by CWDM4 and directed into a balanced photodetector (Thorlabs PDB450C). The generated photocurrents, i_s and i_i, were directly subtracted to yield the difference current i_t. This signal was amplified by a transimpedance amplifier (TIA), low-pass filtered (LPF), and routed to a data acquisition (DAQ) system to measure intensity-difference noise fluctuations. The SNL baseline was calibrated by illuminating the detector with coherent pulses from the same mode-locked laser. A linear fit of the measured noise variance against varying incident optical powers was performed to establish the 0 dB reference, which was then applied to the twin beams by accurately matching their DC photocurrents.

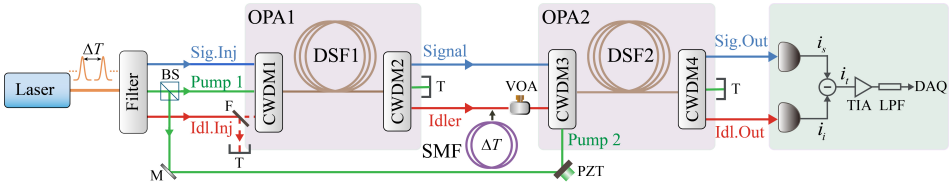


Figure 6. Schematic of the experimental setup based on an all-fiber NLI and a differential detection system. ΔT is the time interval between two adjacent pulses. OPA1-2, optical parametric amplifier; CWDM1-4, coarse wavelength division multiplexing; DSF1-2, dispersion-shifted fiber; SMF, single-mode fiber; BS, beam splitter; F: flip; M, mirror; T, terminator; PZT, piezoelectric transducer; VOA, variable optical attenuator; TIA, transimpedance amplifier; LPF, low-pass filter; DAQ, data acquisition.

We measured the IDS evolution of the output beams as a function of OPA2 pump power across various OPA1 idler intensity gains, controlled by adjusting the respective pump powers P_1 and P_2. During co-injection into OPA2, the seed power of OPA1 was actively adjusted alongside its intensity gain to maintain constant output signal and idler powers of 0.4 μW. The inter-stage transmission efficiencies (η_1 and η_2) were 65% and 67%, while the detection efficiencies (η_s and η_i) were 87% and 85%, respectively. To optimize the electronic gain ratio r for each measurement, we finely tuned the pre-detection transmission efficiencies of the signal and idler beams by mechanically adjusting the fiber coupling and

monitoring the noise variance in real-time to maximize the IDS, which had a negligible impact on the measured squeezing level.

As illustrated in Figure 7, the IDS evolution was measured across OPA1 idler intensity gains of $g_1^2 = 0, 2, 4, 9$, and 27, with the OPA2 pump power (P_2) increasing from 0 to 5 mW. For $g_1^2 = 0$ (P_1 turned off), OPA1 merely transmits the coherent signal and idler fields, rendering OPA2 a PSA with coherent-state injection. As P_1 increases, the fields injected into OPA2 gradually transition into correlated beams. At $P_2 = 0$ mW, the data points reflect the initial degree of correlation from OPA1, which evidently strengthens with higher P_1. In the low-power regime ($P_2 \leq 1$ mW), higher initial correlation yields a stronger final IDS, indicating that the correlation of OPA1 dominates the evolution of the entire system and effectively enhances the squeezing performance. However, as P_2 increases further, the dynamics diverge. Notably, for $P_2 \geq 1$ mW, the IDS for the highest initial correlation ($g_1^2 = 27$) degrades rapidly. Conversely, at $P_2 = 3$ mW, the coherent-state injection ($g_1^2 = 0$) achieves the optimal IDS of -5.85 ± 0.16 dB. For $P_2 > 3$ mW, this disparity amplifies, with high-gain configurations degrading significantly faster than their low-gain counterparts. These dynamics reveal a fundamental competition between the initial correlation, intensity noise, and amplifier gain saturation. While ideal theoretical models suggest that higher injected correlation should unconditionally improve the final IDS, practical cascaded amplification dictates that output intensity noise increases sharply with OPA1 intensity gain. At higher P_2, the excessive initial intensity noise accompanying a high OPA1 intensity gain (e.g., $g_1^2 = 27$) begins to dominate. The superposition of high gains from both OPAs exacerbates gain saturation in OPA2, which impairs quantum interference and severely degrades the measurable squeezing. Consequently, producing high-quality IDS states via cascaded amplifiers cannot solely rely on pursuing highly correlated inputs; mitigating the intensity noise of the injected fields is equally imperative. Ultimately, maximizing the final IDS requires injecting fields with an optimal balance of high correlation and low intensity noise, alongside a precise distribution of gain between the two amplifiers.

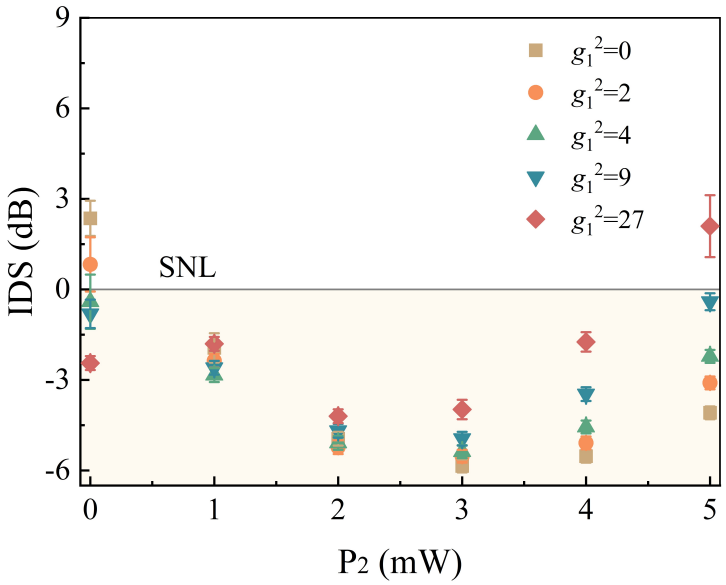


Figure 7. IDS as a function of the average pump power P_2 for various idler intensity gains g_1^2 of OPA1. For the baseline measurement at $g_1^2 = 0$, pump P_1 was turned off, and the coherent signal and idler beams were injected simultaneously into OPA1. As g_1^2 increases ($g_1^2 > 0$), the external idler injection is blocked, and P_1 is turned on. The solid gray line denotes the SNL. Note that the IDS values shown are raw measured data without any loss correction.

Despite precise parameter optimization, the optimal IDS of -5.85 ± 0.16 dB remains inherently constrained by broadband multimode dynamics that extend beyond the single-mode framework. Multimode theory dictates that minimizing intensity-difference noise requires perfect spectral matching between the interacting fields [29]. In practical all-fiber systems, however, high-peak-power pulses induce significant spectral broadening via self-phase and cross-phase modulation, thereby degrading this matching condition. Furthermore, broadband parametric processes exhibit a nonfactorable joint spectral function, distributing quantum correlations across multiple frequency modes. Because the pump pulses undergo independent nonlinear reshaping in each OPA stage, the gain profile of OPA2 cannot perfectly overlap with the multimode quantum state generated by OPA1. Consequently, differential detection integrates over these mismatched modes, effectively averaging down the measurable squeezing. Together with the excess noise of mode-locked lasers, higher-order FWM, and gain saturation, these multimode effects limit the maximum achievable squeezing below the single-mode theoretical predictions.

For practical quantum sensing applications, placing a sample within the NLI inherently introduces inter-stage transmission losses and path delays in the signal and idler arms. First, we investigate the extreme scenario of inter-stage loss by completely blocking the inter-stage idler arm, utilizing a variable optical attenuator (VOA). As previously described, transmission efficiencies were fine-tuned for each measurement to optimize the IDS. By varying P_1, the OPA1 idler intensity gain was set to $g_1^2 = 0, 2, 4, 9$, and 27, transitioning the OPA2 injection from a single-arm coherent state to a single-arm thermal field. Simultaneously, the power of the signal seed for OPA1 was actively adjusted to maintain a constant 0.4 μW injection into OPA2. Figure 8a illustrates the measured IDS as a function of P_2 under these conditions. Across all gains, the squeezing initially improves with P_2, reaches an optimum, and subsequently degrades. Higher OPA1 gains introduce excessive thermal noise, thereby deteriorating the overall squeezing. Optimal squeezing typically occurs at P_2 between 3 and 4 mW; notably, configurations with $g_1^2 = 0$ and 2 achieve squeezing levels approaching -6 dB, consistent with Figure 7. Beyond 4 mW, gain saturation degrades the squeezing across all conditions. Crucially, these results indicate that higher injected thermal noise significantly narrows the optimal P_2 range for sustaining high-quality squeezing.

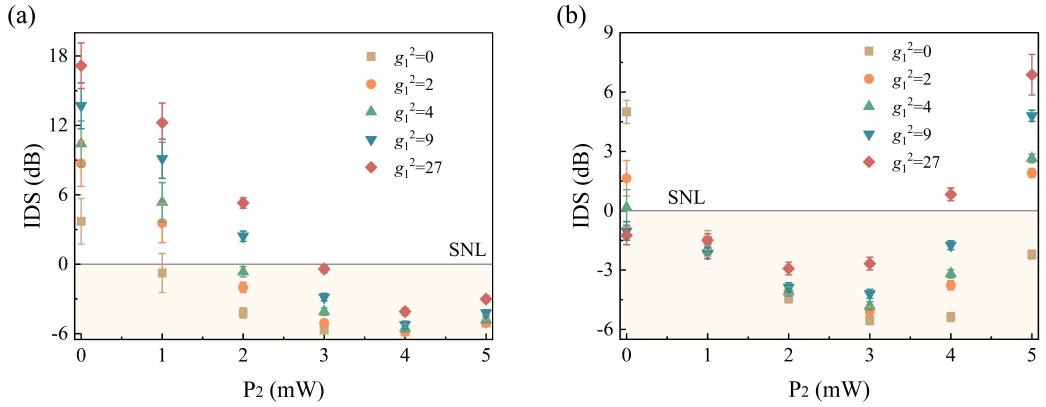


Figure 8. Dependence of the IDS on the average pump power P_2 under different idler intensity gains g_1^2 of OPA1 in the following two cases: (**a**) The idler beam between the two stages is blocked. (**b**) A 4.08 m standard single-mode fiber (SMF) was inserted into the idler arm between the two OPAs to introduce a delay corresponding to one pulse interval. The solid gray line denotes the SNL. Note that the IDS values shown are raw measured data without any loss correction.

Next, we characterized the dependence of the IDS on P_2 by introducing a physical delay of one pulse interval in the inter-stage idler arm. A 4.08 m standard single-mode fiber (SMF) was inserted to emulate the inherent optical path delay caused by a sensing sample.

With g_1^2 again set to 0, 2, 4, 9, and 27, the IDS evolution is presented in Figure 8b. Similar to the blocked-arm scenario, the squeezing exhibits an initial enhancement followed by degradation as P_2 increases. Higher OPA1 intensity gains gradually reduce the maximum achievable IDS, which is attributed to the amplification of delay-induced excess noise. Specifically, introducing a delay of one pulse interval causes the delayed idler and the current signal to originate from independent vacuum fluctuations. This pulse-to-pulse decorrelation introduces uncorrelated excess noise that cannot be fully canceled by standard differential detection, thereby establishing a limit on the achievable squeezing level. The optimal squeezing generally occurs at approximately 3 mW of P_2, approaching -6 dB for low-gain injections ($g_1^2 = 0, 2$). Conversely, extreme intensity gains (e.g., $g_1^2 = 27$) severely limit the optimal squeezing to approximately -3 dB. For $P_2 > 3$ mW, the squeezing degrades uniformly across all conditions due to OPA2 pump depletion, gain saturation, and higher-order FWM generation. These experimental observations align with theoretical predictions [29], confirming that accurate modeling of high-gain fiber parametric devices must incorporate these saturation and higher-order nonlinear mechanisms. Collectively, both sets of results demonstrate a key characteristic: operating OPA1 at a lower gain is essential for maintaining high-quality, stable IDS over a broader P_2 operational range.

4. Summary and Conclusions

In summary, formulated within a single-mode framework, this study presented a theoretical and experimental investigation of the generation and optimization of IDS states within an all-fiber NLI system. We systematically analyzed the physical mechanisms underlying squeezing degradation and revealed that practical imperfections, namely, asymmetric detection efficiencies and inter-stage path delays, trigger severe excess noise mismatches in the high-gain regime. To overcome this bottleneck, we analytically derived and verified an optimal electronic gain ratio that restores system symmetry and effectively compensates for differential photon losses, thereby obtaining optimized squeezing levels across a broad gain range. Furthermore, our experimental results elucidate the complex interplay between the initial field correlation, gain allocation, and pump saturation effects. By demonstrating that maintaining a precisely balanced, lower-gain state in OPA1 is indispensable for mitigating thermal noise, we provide a strategy for parameter optimization. Beyond our specific fiber implementation, this gain–noise trade-off reflects universal design challenges for gain-assisted nonlinear photonic systems. The joint control of gain, nonlinear dynamics, and noise demonstrated here provides a conceptual framework applicable to other architectures, such as active-microcavity solitons where stable frequency comb formation requires similar coordinated optimization [31]. Together, these theoretical insights and experimental demonstrations offer a reliable resolution to noise mismatch issues in cascaded configurations, highlighting the distinctive potential of the NLI as a stable, loss-tolerant architecture for integrated quantum sensing.

While the current single-mode framework successfully isolates the primary physical mechanisms of quantum noise compensation, the intrinsic spatiotemporal dynamics of pulse-pumped parametric processes in optical fibers inherently extend beyond this approximation. As established in multimode theories for single-stage OPA [29], parameters such as the joint spectral function and temporal mode matching strictly govern individual beam noise and final collection efficiency. Although our framework provides an excellent qualitative account of experimental trends, the precise quantitative squeezing levels are further modulated by these multimode effects. Therefore, incorporating these multimode dynamics into the NLI framework is essential for a rigorous quantitative description of realistic all-fiber quantum sensors. Future investigations will expand our theoretical model into the multimode regime to accurately capture these broadband interactions. Ultimately,

building upon the noise compensation strategies and parameter optimization protocols established herein, subsequent research will focus on advancing these integrated interferometric schemes toward practical implementation in precision metrology.

Author Contributions: N.H.: funding acquisition; writing—original draft; writing—review and editing; methodology. X.L.: software; data curation. J.W. (Jinze Wu): formal analysis. J.W. (Jing Wang): funding acquisition; resources. All authors have read and agreed to the published version of the manuscript.

Funding: This work was supported by the National Natural Science Foundation of China (12304402), Fundamental Research Project of Shanxi Province (202303021212212), Taiyuan University of Science and Technology Scientific Research Initial Funding (20232034), and Shanxi Science and Technology Cooperation and Exchange Special Project (202404041101032).

Data Availability Statement: The original contributions presented in this study are included in the article. Further inquiries can be directed to the corresponding author.

Conflicts of Interest: The authors declare no conflicts of interest.

References

1. Giovannetti, V.; Lloyd, S.; Maccone, L. Advances in quantum metrology. *Nat. Photonics* **2011**, *5*, 222–229. [CrossRef]
2. Degen, C.L.; Reinhard, F.; Cappellaro, P. Quantum sensing. *Rev. Mod. Phys.* **2017**, *89*, 035002. [CrossRef]
3. Heng, X.; Zhang, L.; Yin, Q.; Liu, W.; Tang, L.; Zhai, Y.; Wei, K. Quantum-enhanced sensing with squeezed light: From fundamentals to applications. *Appl. Sci.* **2025**, *15*, 10179. [CrossRef]
4. Heidmann, A.; Horowicz, R.; Reynaud, S.; Giacobino, E.; Fabre, C.; Camy, G. Observation of quantum noise reduction on twin laser beams. *Phys. Rev. Lett.* **1987**, *59*, 2555. [CrossRef] [PubMed]
5. Brida, G.; Genovese, M.; Ruo Berchera, I. Experimental realization of sub-shot-noise quantum imaging. *Nat. Photonics* **2010**, *4*, 227–230. [CrossRef]
6. Sabines-Chesterking, J.; McMillan, A.; Moreau, P.; Joshi, S.; Knauer, S.; Johnston, E.; Rarity, J.; Matthews, J. Twin-beam sub-shot-noise raster-scanning microscope. *Opt. Express* **2019**, *27*, 30810–30818. [CrossRef] [PubMed]
7. Dorfman, K.; Liu, S.; Lou, Y.; Wei, T.; Jing, J.; Schlawin, F.; Mukamel, S. Multidimensional four-wave mixing signals detected by quantum squeezed light. *Proc. Natl. Acad. Sci. USA* **2021**, *118*, e2105601118. [CrossRef] [PubMed]
8. Li, T.; Li, F.; Liu, X.; Yakovlev, V.V.; Agarwal, G.S. Quantum-enhanced stimulated brillouin scattering spectroscopy and imaging. *Optica* **2022**, *9*, 959–964. [CrossRef] [PubMed]
9. Pooser, R.C.; Lawrie, B. Ultrasensitive measurement of microcantilever displacement below the shot-noise limit. *Optica* **2015**, *2*, 393–399. [CrossRef]
10. Lawrie, B.J.; Lett, P.D.; Marino, A.M.; Pooser, R.C. Quantum sensing with squeezed light. *ACS Photonics* **2019**, *6*, 1307–1318. [CrossRef]
11. Kwiat, P.G.; Mattle, K.; Weinfurter, H.; Zeilinger, A.; Sergienko, A.V.; Shih, Y. New high-intensity source of polarization-entangled photon pairs. *Phys. Rev. Lett.* **1995**, *75*, 4337. [CrossRef] [PubMed]
12. McCormick, C.; Boyer, V.; Arimondo, E.; Lett, P. Strong relative intensity squeezing by four-wave mixing in rubidium vapor. *Opt. Lett.* **2006**, *32*, 178–180. [CrossRef] [PubMed]
13. Sharping, J.E.; Fiorentino, M.; Kumar, P. Observation of twin-beam-type quantum correlation in optical fiber. *Opt. Lett.* **2001**, *26*, 367–369. [CrossRef] [PubMed]
14. Guo, X.; Li, X.; Liu, N.; Yang, L.; Ou, Z. An all-fiber source of pulsed twin beams for quantum communication. *Appl. Phys. Lett.* **2012**, *101*, 261111. [CrossRef]
15. Zhao, W.; Guo, X.; Li, X. Time-domain measurement of twin beams produced by fiber amplifiers with an ultra-fast pulse train as a pump. *Opt. Lett.* **2023**, *48*, 444–447. [CrossRef] [PubMed]
16. Yurke, B.; McCall, S.L.; Klauder, J.R. SU (2) and SU (1, 1) interferometers. *Phys. Rev. A* **1986**, *33*, 4033. [CrossRef] [PubMed]
17. Ou, Z.; Li, X. Quantum SU (1, 1) interferometers: Basic principles and applications. *APL Photonics* **2020**, *5*, 080902. [CrossRef]
18. Kong, J.; Hudelist, F.; Ou, Z.; Zhang, W. Cancellation of internal quantum noise of an amplifier by quantum correlation. *Phys. Rev. Lett.* **2013**, *111*, 033608. [CrossRef] [PubMed]
19. Jing, J.; Liu, C.; Zhou, Z.; Ou, Z.; Zhang, W. Realization of a nonlinear interferometer with parametric amplifiers. *Appl. Phys. Lett.* **2011**, *99*, 011110. [CrossRef]

20. Tong, Z.; Lundström, C.; Andrekson, P.; McKinstrie, C.; Karlsson, M.; Blessing, D.; Tipsuwannakul, E.; Puttnam, B.; Toda, H.; Grüner-Nielsen, L. Towards ultrasensitive optical links enabled by low-noise phase-sensitive amplifiers. *Nat. Photonics* **2011**, *5*, 430–436. [CrossRef]
21. Manceau, M.; Leuchs, G.; Khalili, F.; Chekhova, M. Detection loss tolerant supersensitive phase measurement with an SU (1, 1) interferometer. *Phys. Rev. Lett.* **2017**, *119*, 223604. [CrossRef] [PubMed]
22. Liu, J.; Wang, Y.; Zhang, M.; Wang, J.; Wei, D.; Gao, H. Ultra-sensitive phase measurement based on an SU (1, 1) interferometer employing external resources and substract intensity detection. *Opt. Express* **2020**, *28*, 39443–39452. [CrossRef] [PubMed]
23. Kalashnikov, D.A.; Paterova, A.V.; Kulik, S.P.; Krivitsky, L.A. Infrared spectroscopy with visible light. *Nat. Photonics* **2016**, *10*, 98–101. [CrossRef]
24. Hudelist, F.; Kong, J.; Liu, C.; Jing, J.; Ou, Z.; Zhang, W. Quantum metrology with parametric amplifier-based photon correlation interferometers. *Nat. Commun.* **2014**, *5*, 3049. [CrossRef] [PubMed]
25. Whittaker, R.; Erven, C.; Neville, A.; Berry, M.; O'Brien, J.; Cable, H.; Matthews, J. Absorption spectroscopy at the ultimate quantum limit from single-photon states. *New J. Phys.* **2017**, *19*, 023013. [CrossRef]
26. Anderson, B.E.; Gupta, P.; Schmittberger, B.L.; Horrom, T.; Hermann-Avigliano, C.; Jones, K.M.; Lett, P.D. Phase sensing beyond the standard quantum limit with a variation on the SU (1, 1) interferometer. *Optica* **2017**, *4*, 752–756. [CrossRef]
27. Yao, B.C.; Wang, W.T.; Xie, Z.D.; Zhou, Q.; Tan, T.; Zhou, H.; Guo, G.C.; Zhu, S.N.; Zhu, N.H.; Wong, C.W. Interdisciplinary advances in microcombs: Bridging physics and information technology. *eLight* **2024**, *4*, 19. [CrossRef]
28. Tan, T.; He, X.Y.; Chang, B.; Guo, X.H.; Zhou, H.; Geng, Y.; Wu, Y.; Liang, Y.P.; Wang, Z.P.; Huang, Y.J.; et al. Biomimetic acoustic perception via chip-scale dual-soliton microcombs. *eLight* **2025**, *5*, 22. [CrossRef]
29. Guo, X.; Li, X.; Liu, N.; Ou, Z. Multimode theory of pulsed-twin-beam generation using a high-gain fiber-optical parametric amplifier. *Phys. Rev. A—At. Mol. Opt. Phys.* **2013**, *88*, 023841. [CrossRef]
30. Ma, R.; Zhang, W.; Wu, X.; Qu, X.; Su, X. High-Bandwidth Intensity-Difference Squeezed State at 895 nm Based on Four-Wave Mixing. *Photonics* **2025**, *12*, 1073. [CrossRef]
31. Liang, Y.; Zhang, D.; Guo, G.; Zhang, H.; Gao, M.; Rao, Y.; Wong, C.W.; Tan, T.; Yao, B. Dissipative Kerr solitons in an active microcavity. *Laser Photonics Rev.* **2026**, *20*, e02552. [CrossRef]

Disclaimer/Publisher's Note: The statements, opinions and data contained in all publications are solely those of the individual author(s) and contributor(s) and not of MDPI and/or the editor(s). MDPI and/or the editor(s) disclaim responsibility for any injury to people or property resulting from any ideas, methods, instructions or products referred to in the content.